

## Research Article

# Metasurface-Based Cylindrical Lenses and Their Antenna Gain Enhancement

Yuping Shang , Wenjun Zhou, and Cheng Liao

*Institute of Electromagnetics, School of Physical Science and Technology, Southwest Jiaotong University, Chengdu 610031, China*

Correspondence should be addressed to Yuping Shang; shangyuping530@sina.com

Received 23 June 2020; Revised 25 August 2020; Accepted 7 September 2020; Published 21 September 2020

Academic Editor: Giorgio Montisci

Copyright © 2020 Yuping Shang et al. This is an open access article distributed under the Creative Commons Attribution License, which permits unrestricted use, distribution, and reproduction in any medium, provided the original work is properly cited.

Electromagnetic metasurface lenses with the characteristic of being conformal to a cylindrical geometry are presented in this study. Based on the formulated principle of the cylindrical metasurface lens operating with transmission or reflection mode, the transmission or reflection phase gradient varying along the circumferential direction of a cylinder is implemented. A focused beam is observed at the objective focal point for each lens illuminated by a plane electromagnetic wave with transverse magnetic or transverse electric polarization. A coaxial-fed microstrip patch antenna element is used as a feeding of cylindrical metasurface lenses and positioned at their focal points, so as to evaluate their application in the enhancement of antenna gain along the boresight direction. By virtue of the focusing ability of presented lenses, effectively enhanced boresight gain from the cylindrical metasurface lens antennas are obtained, in comparison with the freestanding feeding antenna. The agreement between simulation and measurement validates the designs. Conformal integration or embedment of the electromagnetic lens into a certain platform skin with cylindrical characteristics is therefore potentially demonstrated, which implies an enhancement of boresight gain without obviously disturbing the local shape of the skin by apparent weight or drag.

## 1. Introduction

Electromagnetic lens has found wide applications in the gain enhancement of various antennas, due to its ability to transform a nonplanar wavefront into a planar one. The traditional electromagnetic lens mainly relies on its transition of medium parameter and shape to alter the electric path length and thus to achieve the phase compensation necessary for the wavefront transformation [1–3], which usually leads to the thick profile along the wave propagating direction and the associated weight. The resultant bulkiness may limit the conformal integration of the traditional lens with the curved surfaces of certain platforms. Recently, metasurface was studied with the flexibility in manipulating refraction and reflection. Based on the generalized laws of refraction and reflection [4, 5], local modification of wave characteristics serves as the basis of manipulation. The passive metasurface has been designed for different applications ranging from optical wave to microwave, such as abnormal refraction and reflection [6, 7], radar cross-section

reduction [8–10], polarization conversion [11, 12], beam-splitter [13], beam-focusing [14–21], and lens antennas [22–33]. The section thickness of the metasurface is small relative to its operating wavelength. As a result, the lens based on metasurface can collimate the incident beam with a very low profile, which can facilitate the lightweight as well as the integration of the lens.

Depending on the manipulation of refraction or reflection, the reported electromagnetic metasurface lens can be classified as transmission type (T-type) or reflection type (R-type). For both types of operation, a feeding antenna is typically fixed at the focal point of the metasurface lens so that the whole structure can function as a lens antenna. Compared with the freestanding feeding antenna, the lens antenna results in radiation enhancement through the redistributed aperture. For the T-type operation, a flat metasurface lens with a circular shape of  $16.2\lambda$  diameter increases the gain of a horn antenna by 13 dB at 11.3 GHz, where  $\lambda$  is the free space wavelength at the operating frequency of the lens [25]. A four-layered metasurface lens with

a square shape of  $4.3\lambda$  side length helps to improve the gain of a microstrip patch antenna by 11.6 dB at 10 GHz [26]. Similarly, the gain of a microstrip patch antenna is increased by 8.2 dB at 10 GHz by the use of a dual-layered metasurface lens with a square shape of  $3.46\lambda$  side length [27]. A dual-band metasurface lens operates within C-band for  $y$ -polarization and X-band for  $x$ -polarization [28]. Using a Vivaldi antenna as the feeding antenna, the gain increase is 13.1 dB at 6.5 GHz and 13.8 dB at 10.5 GHz. On the other hand, an offset-fed planar reflector antenna based on R-type metasurface lens was designed [29]. Using a horn antenna for feeding, the metasurface-based planar reflector antenna shows a boresight gain similar to the traditional parabolic antenna with the same aperture at 10 GHz. A Vivaldi antenna feeds a reflection-type metasurface lens, which gives rise to 11.1 dB gain enhancement at 10 GHz [30]. A metasurface lens operating in reflection or transmission type for different frequencies was reported with at least 7 dB enhancement of a Vivaldi feeding antenna gain [31]. In addition, a dual-function metasurface lens can operate in reflection or transmission type for different linear polarizations at the same frequency [32]. Fed with a Vivaldi antenna, 10.33 dB and 11.73 dB gain increases were achieved for reflection- and transmission-type operation at 10 GHz, respectively. Similarly, a metasurface lens operates with reflection type for  $y$ -polarization at 10 GHz and transmission type for  $x$ -polarization at 14 GHz [33]. Compared with the Vivaldi feeding antenna, the gain is increased by 8.6 dB at 10 GHz and 8.4 dB at 14 GHz. It is noted that reported metasurface lens antennas were mostly designed through planar metasurfaces with flat geometry. In view of the increasing application where conformal installation of the antenna onto the platform body is desired, design of conformal lens antennas through curved metasurfaces is of practical significance. Curved metasurfaces have been studied for scattering reduction [34, 35], backscattering enhancement [36], and conformal cloaks [37–39] while lens antennas based on curved metasurfaces have been seldom reported.

With an aim of demonstrating the conformal integration or embedment of the lens into the cylindrical structure, passive metasurfaces conformal to a cylindrical geometry are employed to implement curved lens antennas in this study. Since the cylindrical structure is typically involved in many moving platform bodies, the conformal integration or embedment of the lightweight lens into the curved platform skin can potentially lend the lens itself to be a part of the platform body. In such a case, the local shape of the platform skin can remain unchanged, and thus, enhanced radiation can be probably obtained without obviously increasing the air drag, while directly integrating the traditional lens or planar metasurface lens onto the cylindrical skin tends to incur increased drag and disturbed aerodynamics. Initially, a cylindrical metasurface lens operating with T-type or R-type for both transverse magnetic (TM) and transverse electric

(TE) polarizations is designed. The phase gradient of the metasurface lens and its angular sampling for calculating the phase distribution are formulated along the circumferential direction of the cylinder. An etched slot is used to constitute the four-layer unit cell, and slot dimensions are varied to achieve the transmission phase gradient for the T-type cylindrical metasurface lens, while a printed copper loop is used as the unit cell, and its outer or inner edge length is changed to attain the reflection phase gradient for the R-type cylindrical metasurface lens. Then, a dual-polarized microstrip patch antenna element is deployed as the feeding antenna of designed lenses to mainly investigate the boresight gain enhancement. By virtue of the focusing ability of cylindrical metasurface lenses, effective enhancement of boresight gain is observed from the T-type or R-type cylindrical metasurface lens antenna, in comparison with the freestanding feeding antenna.

## 2. Focusing Principle

### 2.1. Phase Gradient of Cylindrical Metasurface Lens

*2.1.1. T-type.* The T-type cylindrical metasurface lens that can focus an incident plane electromagnetic wave is formulated in this section. Figure 1(a) presents a cross-sectional view of the cylindrical geometry considered. The center of the circular profile coincides with the origin  $O$  of the coordinate system. The axis of the cylinder made of dielectric material lies in the  $z$ -axis. A thin dielectric substrate with relative permittivity  $\epsilon_{r1}$  and thickness  $h_1$  wrapping around the dielectric cylinder is used to support unit cells of the lens. A plane electromagnetic wave propagating from  $+x$  to  $-x$  direction illuminates the geometry. This illumination directly covers the upper half of the cylindrical surface with the central angle  $\alpha$  correspondingly ranging from  $-90^\circ$  to  $+90^\circ$ . The T-type cylindrical metasurface lens is thus situated within that coverage. It is noted that each position  $P$  within that coverage experiences an angle of incidence  $\theta_i$  equal to its corresponding central angle  $\alpha$ . The objective of the T-type cylindrical metasurface lens is to refract the incident ray for each position  $P$  to the focal point  $F$ . The focal point  $F$  is selected to be collocated with the center of the circular profile, and air is used as the dielectric material of the cylinder for simplicity. Therefore, the refracted ray coinciding with the local normal indicates that the angle of refraction  $\theta_t$  keeps zero for every position  $P$  within that coverage, although the angle of incidence  $\theta_i$  changes for different positions. With the determined angles of incidence and refraction, the transmission phase gradient of the cylindrical metasurface lens is obtained through the generalized law of refraction as

$$\frac{d\Psi_t}{d\alpha} = \frac{2\pi(R_t + h_1)}{\lambda_0} \sin(|\theta_i|), \quad (1)$$

where  $\lambda_0$  is the free space wavelength of the incident plane electromagnetic wave and  $R_t$  is the radius of the air cylinder. With  $\lambda_0 \approx 30$  mm at 10 GHz,  $R_t = 150$  mm ( $5 \lambda_0$ ), and

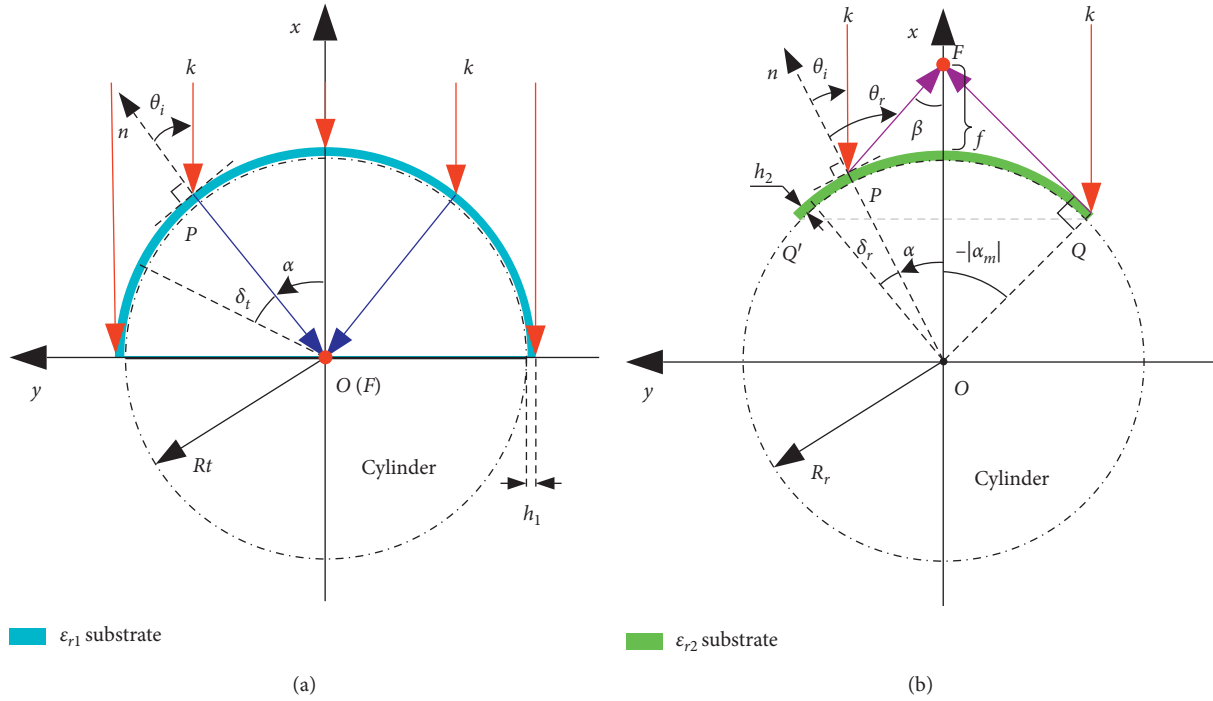


FIGURE 1: Cross-sectional view of the cylindrical geometry considered for the lens operating in (a) T-type or (b) R-type. Arbitrary position  $P$  on the cylindrical surface can be characterized by its corresponding central angle  $\alpha$  formed between  $+x$  axis and  $OP$ . At position  $P$ , its angle of incidence  $\theta_i$  is formed between the local outward-pointing normal  $n$  and the incident wave vector  $k$ . The angular interval between adjacent sampling positions is denoted as  $\delta$ .

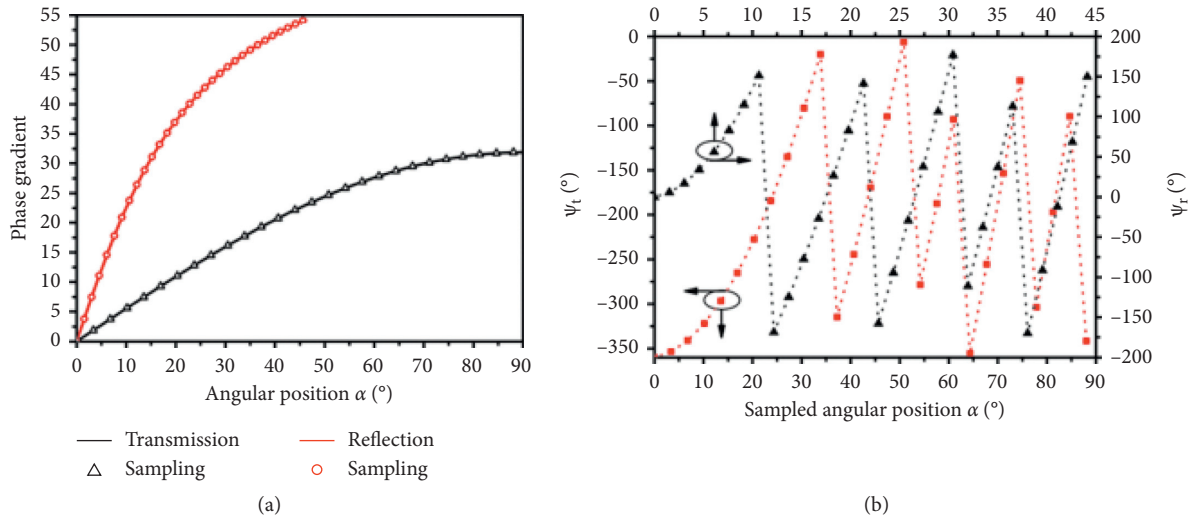


FIGURE 2: Calculated (a) phase gradient and (b) phase distribution for the T-type or R-type cylindrical metasurface lens.

$h_1 = 2.286 \text{ mm}$  ( $0.076 \lambda_0$ ), the transmission phase gradient is calculated and plotted in Figure 2(a). Due to the geometrical symmetry about the  $x$ -axis, only half of the metasurface lens coverage is displayed on the horizontal axis of Figure 2(a).

**2.1.2. R-type.** Figure 1(b) illustrates the cylindrical geometry considered for the R-type lens. The relative relationship among the coordinate system, circular profile,

and incident plane electromagnetic wave remains unchanged, while the focal point  $F$  toward which the R-type cylindrical metasurface lens reflects the incident rays is located outside the circular profile. The radius of this cylinder is denoted as  $R_r$ . A thin dielectric substrate with relative permittivity  $\epsilon_{r2}$  and thickness  $h_2$  surrounding the partial surface of the cylinder is similarly used to carry unit cells of the lens. Thus, there is a distance  $(R_r + h_2 + f)$  existing between the origin  $O$  and the focal point  $F$ . For a

specified  $f$ , it is noticed that the reflected ray at position  $Q$  corresponding to a central angle  $-|\alpha_m|$  is tangential to the circular profile. Due to the structural symmetry with respect to the  $x$ -axis, another position  $Q'$  with the central angle  $|\alpha_m|$  appears in the first quadrant. Since the line connecting any point whose  $\alpha < -|\alpha_m|$  or  $\alpha > |\alpha_m|$  and the focal point  $F$  would intersect the circular profile, the considered coverage of the cylindrical metasurface lens operating in reflection mode ranges from  $-|\alpha_m| \leq \alpha \leq |\alpha_m|$ , although the upper half of the cylindrical surface is directly illuminated by the incident wave. The angle of incidence  $\theta_i$  for each position  $P$  is also equal to the corresponding central angle  $\alpha$ . For the purpose of focalization at  $F$ , each position  $P$  within the coverage of the cylindrical metasurface lens needs to reflect with an angle of reflection  $\theta_r$  equal to

$$\begin{aligned}\theta_r &= -(|\theta_i| + |\beta|), \\ \beta &= \arctan \left\{ \frac{(R_r + h_2) \sin(|\theta_i|)}{f + (R_r + h_2) [1 - \cos(|\theta_i|)]} \right\}, \\ \alpha_m &= \arccos \left( \frac{R_r + h_2}{R_r + h_2 + f} \right).\end{aligned}\quad (2)$$

By substituting the determined angles of incidence and reflection into the generalized laws of reflection, the reflection phase gradient of this cylindrical metasurface lens is expressed as follows:

$$\frac{d\Psi_r}{d\alpha} = \frac{2\pi(R_r + h_2)}{\lambda_0} [\sin(|\theta_i|) - \sin \theta_r]. \quad (3)$$

Calculated with  $\lambda_0 \approx 30$  mm,  $f = 60$  mm ( $2 \lambda_0$ ),  $R_r = 150$  mm ( $5 \lambda_0$ ), and  $h_2 = 0.635$  mm ( $0.021 \lambda_0$ ), the reflection phase gradient is also shown in Figure 2(a). It is seen that the coverage of this cylindrical metasurface lens corresponds to  $-44.34^\circ \leq \alpha \leq 44.34^\circ$  for the specified geometrical dimensions.

## 2.2. Phase Distribution of Cylindrical Metasurface Lens.

In order to map the calculated phase gradient onto the cylindrical surface, the unit cell involving a certain periodicity is utilized to constitute the lens. As a result of the discrete unit cell, the continuously varying angle of incidence as well as phase gradient of the metasurface lens has to be sampled along the circumferential direction of the cylinder with an angular interval  $\delta$ .

**2.2.1. T-type.** Based on the transmission phase gradient of the T-type lens, the dimensions of the  $n$ -th unit cell are determined according to the variation of transmission phase  $\Psi_t$  between neighboring unit cells as follows:

$$\Psi_{t(n)} = \Psi_{t(n-1)} + \frac{2\pi(R_t + h_1)}{\lambda_0} \sin(|\theta_{i(n)}|) \cdot \delta_t, \quad (4)$$

where  $n$  is an integer number ranging from 2 to  $(90^\circ/\delta_t)$ ,  $\delta_t = (360 \times p_{c1})/[2\pi \times (R_t + h_1)]$ , and  $p_{c1}$  is the unit cell periodicity along the circumferential direction of the cylinder.

Using  $p_{c1} = 9$  mm ( $0.3 \lambda_0$ ), the sampled angular position and corresponding transmission phase gradient are indicated in Figure 2(a). Depending on the sampled gradient, the transmission phase distribution for sampled angular positions is calculated as shown in Figure 2(b). The transmission phase for the first unit cell is specified as  $\Psi_{t(1)} = -360^\circ$  at the position  $\alpha = 0^\circ$ .

**2.2.2. R-type.** For the R-type cylindrical metasurface lens, the dimensions of the  $n$ -th unit cell can be similarly obtained through the variation of reflection phase  $\Psi_r$  between adjacent unit cells

$$\Psi_{r(n)} = \Psi_{r(n-1)} + \frac{2\pi(R_r + h_2)}{\lambda_0} [\sin(|\theta_{i(n)}|) - \sin \theta_{r(n)}] \delta_r, \quad (5)$$

where  $n$  is an integer number ranging from 2 to  $(\alpha_m/\delta_r)$ ,  $\delta_r = (360 \times p_{c2})/[2\pi \times (R_r + h_2)]$ , and  $p_{c2}$  is the unit cell periodicity along the circumferential direction of the cylinder.

With the circumferential periodicity of the unit cell  $p_{c2} = 4$  mm ( $0.13 \lambda_0$ ), Figure 2(a) also exhibits the sampled angular position and corresponding reflection phase gradient. Relying on the sampled gradient, the reflection phase distribution for sampled angular positions is shown in Figure 2(b). The reflection phase for the first unit cell is specified as  $\Psi_{r(1)} = 0^\circ$  at the position  $\alpha = 0^\circ$ .

## 2.3. Unit Cell Dimensions of Cylindrical Metasurface Lens

**2.3.1. T-type.** According to the transmission phase limit of multilayered frequency-selective surfaces [40], a unit cell containing four layers is used to achieve the transmission phases in Figure 2(b). Figure 3 shows the four-layer unit cell geometry with a square lattice. Each layer contains an etched slot. Four layers of the unit cell share the same geometrical dimensions and are separated from each other by a thin dielectric substrate Taconic RF-30 with relative permittivity  $\epsilon_{r1} = 3$ , dielectric loss tangent 0.0014, and thickness  $h_1/3 = 0.762$  mm. The unit cell is simulated with periodic boundaries and the  $xz$ -plane in Figure 3 is deemed as the plane of incidence. It is known that the transmission responses for normal incidence of TM and TE polarizations are identical when  $d_{iy} = d_{iz}$ , due to the rotational symmetry with respect to the  $x$ -axis. With  $p_{c1} = 9$  mm and  $t = 0.2$  mm, Figure 4(a) plots the transmission response of the flat periodic array under normal incidence with  $\theta_i = 0^\circ$  at 10 GHz. It is seen that the transmission phase range of  $360^\circ$  with a

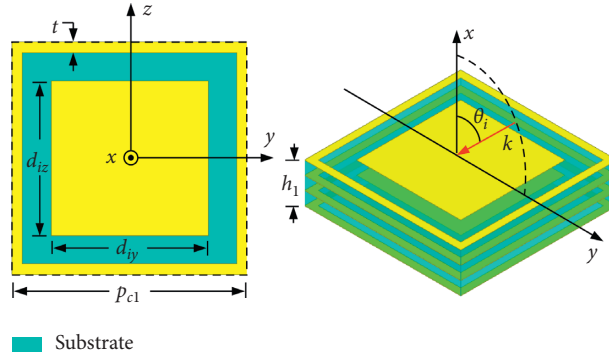


FIGURE 3: The utilized unit cell geometry for the T-type cylindrical metasurface lens.

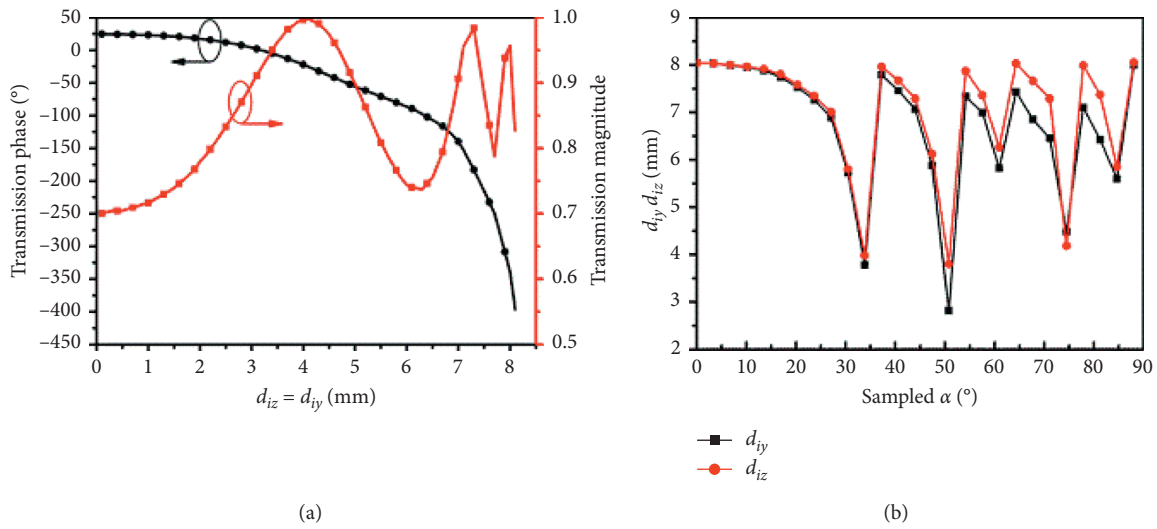


FIGURE 4: Simulated (a) transmission phase and magnitude of the unit cell and (b) edge lengths of the inner patch at every sampled position.

magnitude bigger than 0.73 can be obtained by varying the edge length of the inner patch, which implies this unit cell can be used to establish the sampled transmission phases for different positions in Figure 2(b) and thus the gradient via variation in  $d_{iy}$  or  $d_{iz}$ .

Since the transmission responses for TM and TE polarizations diverge for oblique angle of incidence, the slight difference between  $d_{iy}$  and  $d_{iz}$  is adopted to achieve the same transmission phase for both polarizations at sampled positions under oblique incidence in Figure 2(b). TM and TE responses are mainly affected by  $d_{iz}$  and  $d_{iy}$ , respectively. The obtained edge lengths at every sampled position are plotted in Figure 4(b). Because the adjustment of physical dimensions in simulation can only be conducted with a finite step length, the simulated transmission phases for both polarizations at every sampled position may not be exactly equal to the calculated value, and the deviation between simulation and calculation is observed within  $\pm 6^\circ$  for most angles of incidence.

2.3.2. *R-type*. To obtain the same reflection phase for both polarizations at sampled positions under oblique incidence, the copper loop geometry slightly modified with rectangular outer or inner contour is used as the unit cell to build the R-type cylindrical metasurface lens [36]. As seen in Figure 5, the copper loop is printed on the upper side of a grounded dielectric substrate Taconic RF-10 with relative permittivity  $\epsilon_{r2}=10.2$ , dielectric loss tangent 0.0025, and thickness  $h_2=0.635$  mm. Similarly, the  $xz$ -plane is taken as the plane of incidence. The reflection response of the geometry under oblique incidence of TM (TE) polarization is mainly influenced by  $d_{iy}$  and  $d_{oz}$  ( $d_{iz}$  and  $d_{oy}$ ). Using the calculated reflection phases at sampled positions in Figure 2(b) as the objective values, simulation is conducted to find dimensions of the loop unit cell at every sampled position, and results are plotted in Figure 6. Because of the accuracy of dimension adjustment, the deviation between the simulated and calculated reflection phases is within  $\pm 3^\circ$  for most angles of incidence.

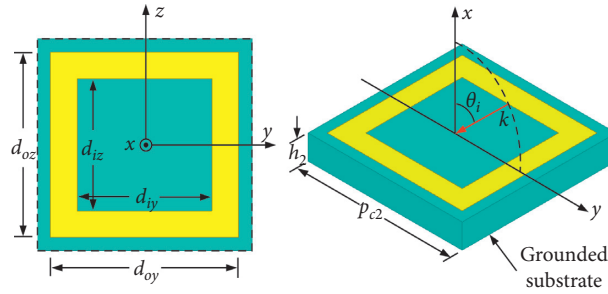


FIGURE 5: The utilized unit cell geometry for the R-type cylindrical metasurface lens.

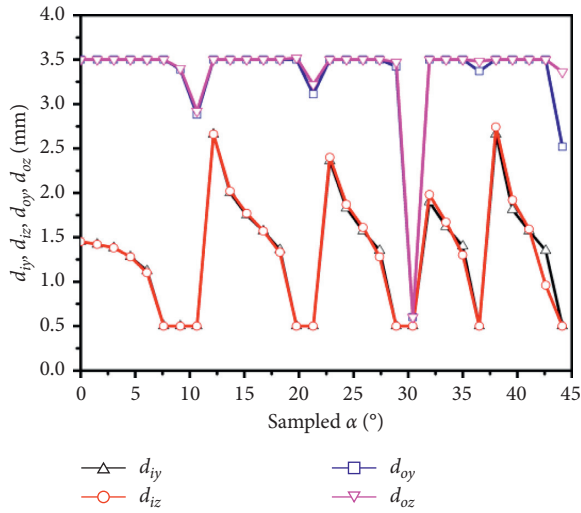


FIGURE 6: Dimensions of the loop unit cell at every sampled position.

### 3. Cylindrical Metasurface Lens Antennas

#### 3.1. Beam-Focusing Results

**3.1.1. T-type.** With the determined dimensions in Figure 4(b), the unit cells are then conformally laid onto the cylindrical surface to obtain an array functioning as the cylindrical metasurface lens. While air cylinder is considered during analysis for simplicity, a semicylinder made of polymethacrylimide foam with relative permittivity 1.067 is employed to support the lens, as seen in Figure 7. The unit cells circumferentially coat the cylindrical surface, and they are duplicated along the  $z$ -axis, so that the T-type cylindrical metasurface lens is obtained. The height of the cylinder is  $h_t = 90$  mm ( $3\lambda_0$ ) which can accommodate ten unit cells along the  $z$ -axis. A plane electromagnetic wave propagating from  $+x$  to  $-x$  direction illuminates the structure. The simulated magnitude of electric field  $E_y$  and power density for TE-polarized plane wave incidence at 10 GHz are presented in Figures 8(a)–8(d). The electric field and power density concentrated around the objective focal point suggest the refraction-based beam focusing of the T-type cylindrical metasurface lens. A similar focusing result can be seen from Figures 8(e)–8(h) for TM-polarized plane wave

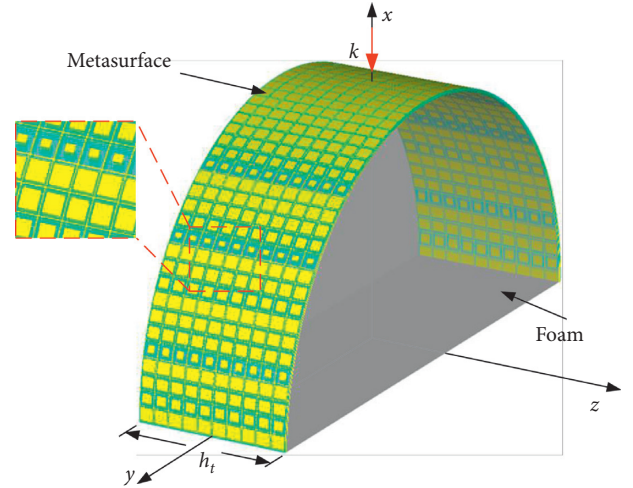


FIGURE 7: Foam semicylinder coated with the T-type cylindrical metasurface lens.

incidence. Besides, through a 10% variation in all parameters of the unit cell including  $t$ ,  $d_{iz}$ ,  $d_{iy}$ ,  $h_1$ , and  $p_{c1}$ , it is found that the focusing electric field result is sensitive to this variation of  $d_{iz}$ ,  $d_{iy}$ , and  $p_{c1}$ , while the remaining parameters cause little influence on the focusing electric field result.

**3.1.2. R-type.** Analogically, the loop unit cells with determined dimensions in Figure 6 circumferentially cover a cylindrical surface, and they are duplicated along the  $z$ -axis to obtain the R-type cylindrical metasurface lens, as seen in Figure 9. A copper cylinder is used to support this lens. Because of the grounded substrate of this lens, it may be mentioned that a dielectric cylinder may also reside below this lens. The height of the cylinder is  $h_r = 60$  mm ( $2\lambda_0$ ), and fifteen unit cells are distributed along the  $z$ -axis. With the illumination of a plane electromagnetic wave coming from  $+x$  direction, the simulated magnitude of electric field  $E_y$  and power density are shown in Figures 10(a)–10(d) for TE polarization and Figures 10(e)–10(h) for TM polarization at 10 GHz. The focused beam around the objective focal point indicates the effective occurrence of this reflection-based focusing. According to a similar 10% variation in unit cell parameter values ( $d_{oz}$ ,  $d_{oy}$ ,  $d_{iz}$ ,  $d_{iy}$ ,  $h_2$ , and  $p_{c2}$ ), sensitive parameters are found out to be  $d_{oz}$ ,  $d_{oy}$ , and  $p_{c2}$ .

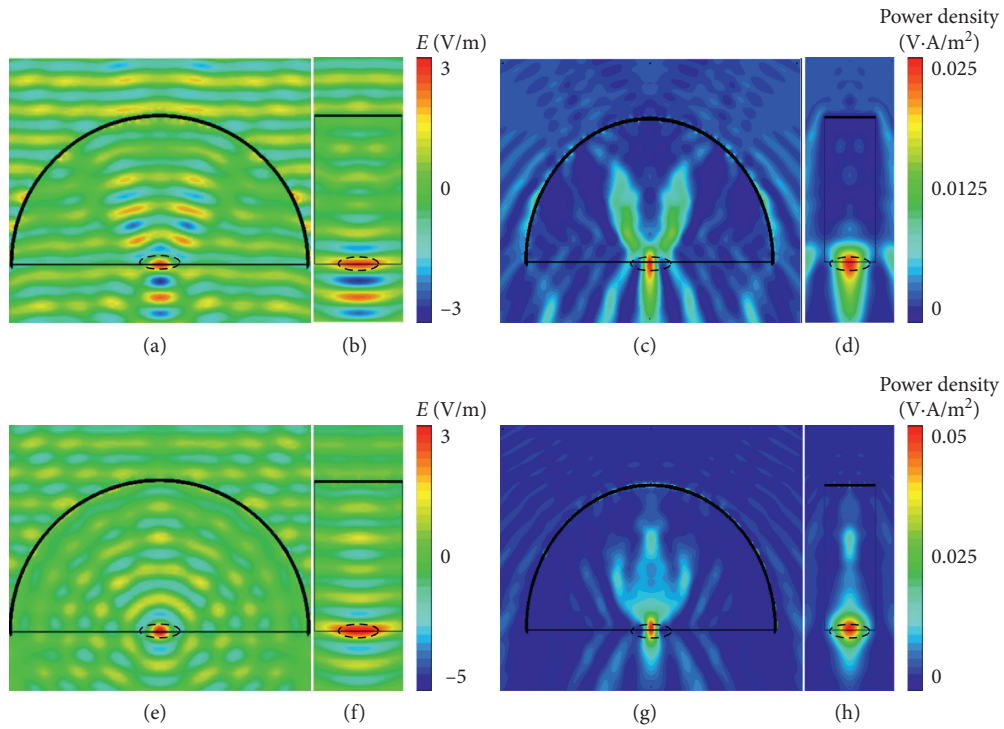


FIGURE 8: Simulated magnitude of electric field  $E_y$  in (a)  $xy$ - and (b)  $xz$ -planes and power density in (c)  $xy$ - and (d)  $xz$ -planes for TE-polarized incidence; magnitude of electric field  $E_z$  in (e)  $xy$ - and (f)  $xz$ -planes and power density in (g)  $xy$ - and (h)  $xz$ -planes for TM-polarized incidence, at 10 GHz.

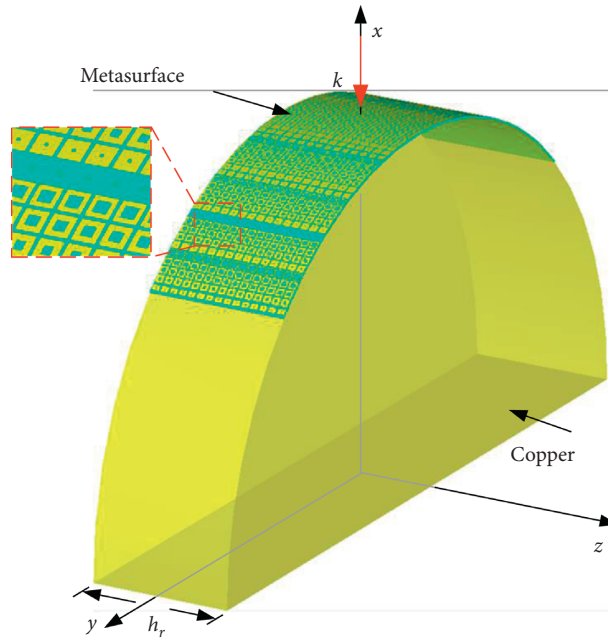


FIGURE 9: Copper semicylinder coated with the R-type cylindrical metasurface lens.

3.2. *Enhanced Boresight Gain.* Based on the beam-focusing effect produced by the T-type or R-type cylindrical metasurface lens, a feeding antenna can be placed at the focal point of the lens, with the aim of enhancing its boresight gain. Due to the narrow-band operation of the lenses, a

probe-fed microstrip patch antenna element is simply designed to have the fundamental resonance at 10 GHz and used as the feeding antenna of both lenses to evaluate the enhancement performance. Other types of antennas may also be used as a feeding antenna of the lenses.

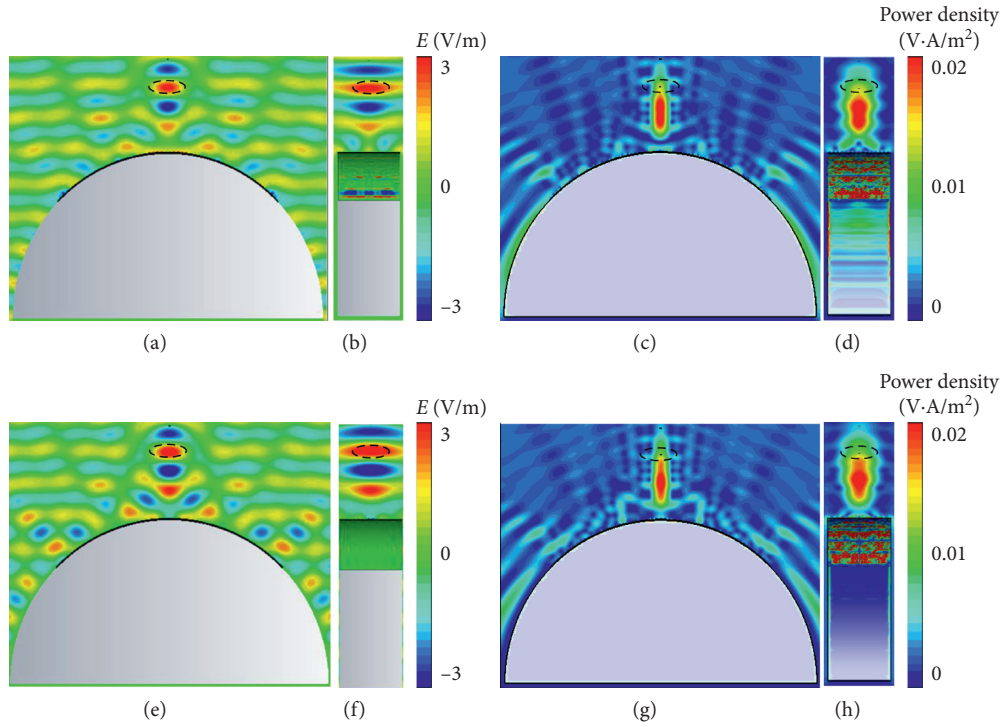


FIGURE 10: Simulated magnitude of electric field  $E_y$  in (a)  $xy$ - and (b)  $xz$ -planes and power density in (c)  $xy$ - and (d)  $xz$ -planes for TE polarization; magnitude of electric field  $E_z$  in (e)  $xy$ - and (f)  $xz$ -planes and power density in (g)  $xy$ - and (h)  $xz$ -planes for TM polarization, at 10 GHz.

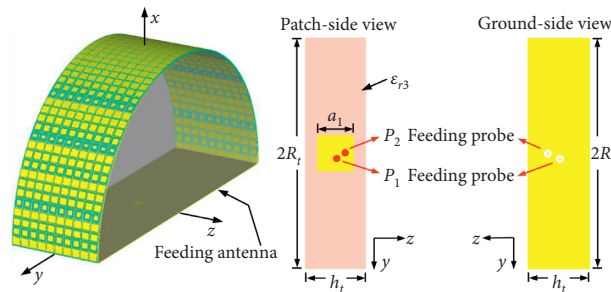


FIGURE 11: T-type cylindrical metasurface lens fed with a microstrip square patch antenna element.

3.2.1. *T-type*. Figure 11 depicts the microstrip patch antenna element that feeds the T-type lens. The commercial laminate Taconic TLY-5 with relative permittivity  $\epsilon_{r3} = 2.2$ , dielectric loss tangent 0.001, and thickness 0.787 mm is used as the dielectric substrate of the patch antenna element. Two excitation probes  $P_1$  and  $P_2$  are incorporated for the square patch with  $a_1 = 9.32$  mm to generate the radiating waves with TE and TM polarizations relative to the cylindrical lens, respectively. For the freestanding microstrip patch antenna, its simulated magnitudes of input reflection coefficients for  $P_1$  and  $P_2$  excitation probes are plotted in Figures 12(a) and 12(b), respectively. The patch center coincides with the designed focal point and Figures 12(a) and 12(b) also show simulated magnitudes of input reflection coefficients of the microstrip patch antenna situated below the lens for a comparison. The comparison of main lobe gain and radiation efficiency varying with frequency is presented in

Figures 12(c) and 12(d). The fundamental resonance frequency very close to 10 GHz is observed for both the feeding antenna and lens antenna. Due to the transformed wavefront, obviously enhanced main lobe gain relative to the feeding antenna is generated from the lens antenna around 10 GHz. Meanwhile, the lens antenna operates with a radiation efficiency of 80.79% and 85.47% at 10 GHz for TE and TM polarizations, respectively.

Moreover, the realized gain of the cylindrical metasurface lens antenna is compared with that of the freestanding feeding antenna at 10 GHz in Figure 13. It is seen from Figures 13(a) and 13(b) that the realized gain along the boresight direction is enhanced from 7.12 dBi of the freestanding microstrip patch antenna to 18.35 dBi of the cylindrical metasurface lens antenna. A 11.23 dB enhancement of the boresight gain is thus obtained for TE-polarized radiation. For TM-polarized radiation in Figures 13(c) and 13(d), the boresight gain is

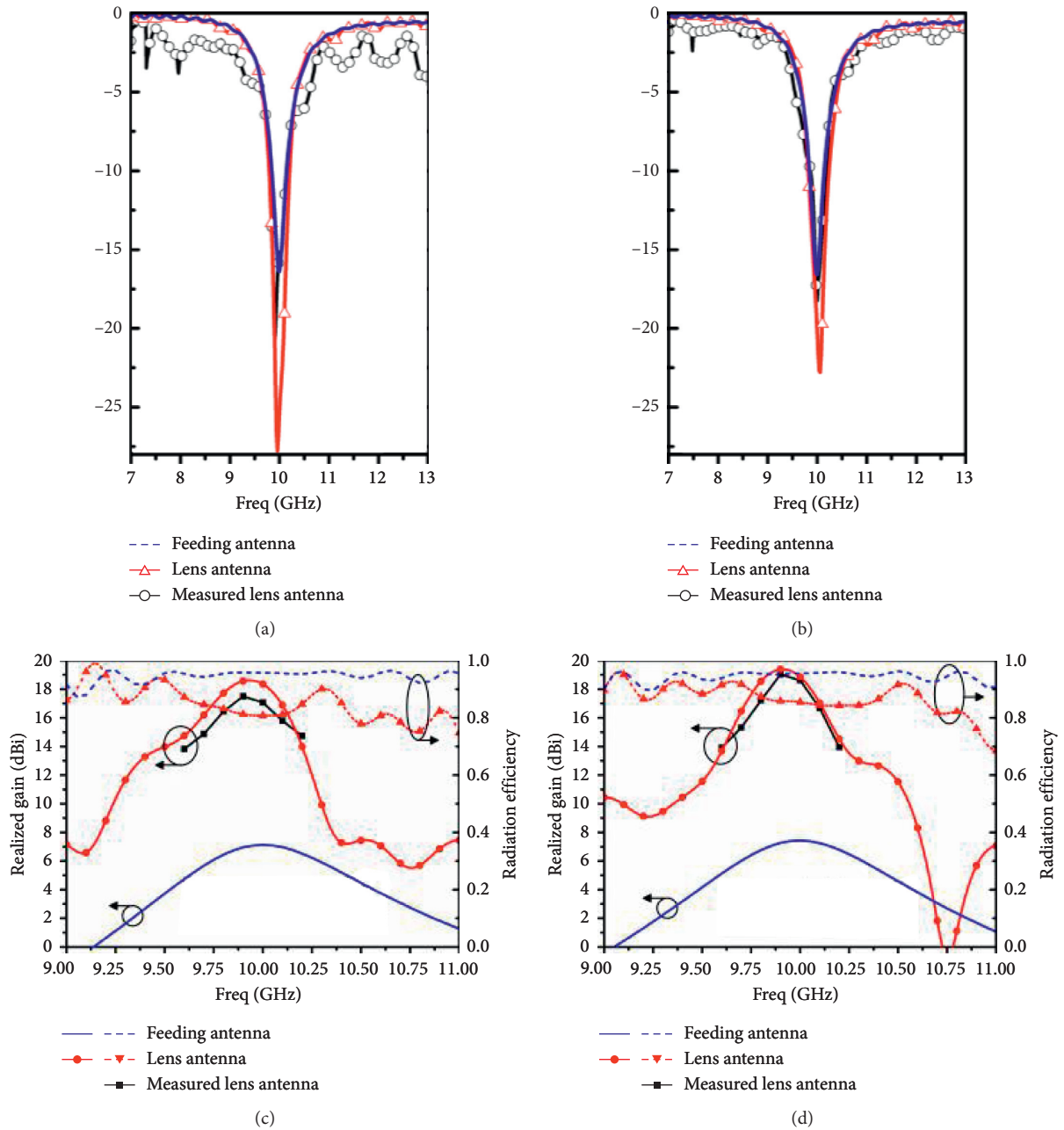


FIGURE 12: Frequency-dependent magnitudes of input reflection coefficients, main lobe gain, and radiation efficiency of the freestanding microstrip patch antenna element and the T-type cylindrical metasurface lens antenna. (a, c) TE-polarized radiation. (b, d) TM-polarized radiation.

increased by 11.44 dB from 7.42 dBi of the freestanding feeding antenna to 18.86 dBi of the cylindrical metasurface lens antenna. Because the cylindrical lens achieves the transmission phase gradient only along the circumferential direction of the cylinder and maintains uniformity along the axial direction of the cylinder, it is also noted in Figure 13 that the patterns in the  $xz$ -plane containing the cylinder axis exhibit obvious first side lobes with magnitudes about 8 dB smaller than the main lobe peak for both polarizations. This may be alleviated by introducing a certain gradient for the

focusing effect along the axial direction through the complete expression of generalized refraction law [5].

3.2.2. *R-type*. The cylindrical metasurface lens antenna operating in R-type is shown in Figure 14. Dimensions of the square patch element and ground of the feeding antenna are  $a_2 = 9.32$  mm and  $b_2 = 15$  mm, respectively. Magnitudes of input reflection coefficients of both the feeding antenna and lens antenna are shown in Figure 15(a) for TE polarization

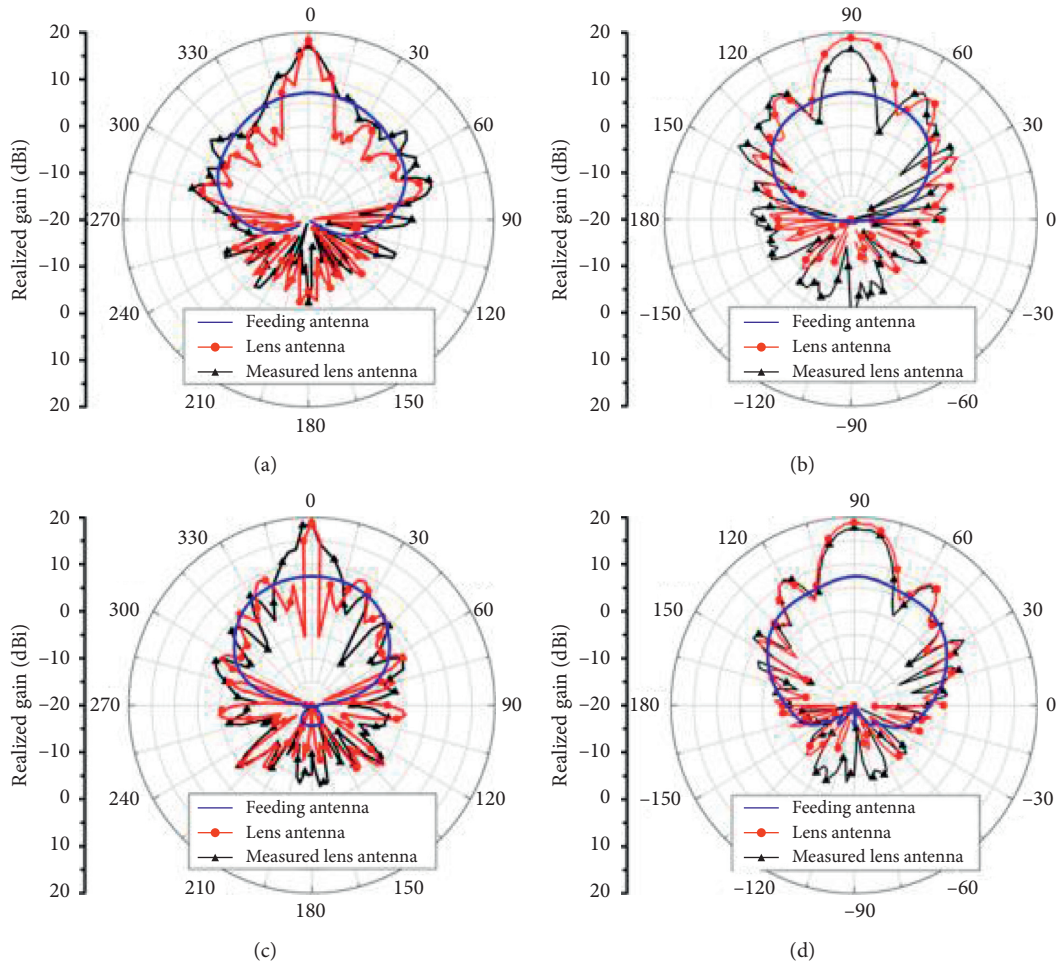


FIGURE 13: Two-dimensional radiation patterns of the freestanding microstrip patch antenna element and the T-type cylindrical metasurface lens antenna. (a)  $xy$ - and (b)  $xz$ -planes for TE-polarized radiation and (c)  $xy$ - and (d)  $xz$ -planes for TM-polarized radiation.

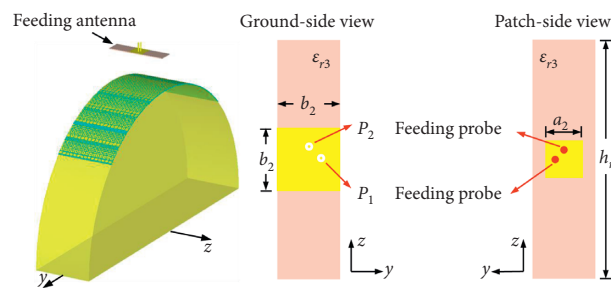


FIGURE 14: R-type cylindrical metasurface lens fed with a microstrip square patch antenna element.

and in Figure 15(b) for TM polarization, which indicates the operating frequency around 10 GHz. As can be seen from Figures 15(c) and 15(d), the lens antenna produces augmented boresight gain relative to the feeding antenna around 10 GHz with a radiation efficiency of 85.24% and 85.32% for TE and TM polarizations, respectively. Similarly, radiation patterns of both antennas at 10 GHz are compared in Figures 16(a)–16(d). Due to the operating manner, the main lobe direction of the feeding antenna orients to the

back lobe direction of this eventual lens antenna, and only partial area of the upper half cylindrical surface is covered with the unit cells of the lens. Thus, obvious radiation towards the backward direction of this eventual lens antenna is noted. It is seen that the boresight gain is increased by 5.92 (5.83) dB from 6.96 (7) dBi of the feeding antenna to 12.88 (12.83) dBi of the lens antenna for TE- (TM-) polarized radiation. On account of the orientation of the feeding antenna, lobes in the backward half-space of this lens

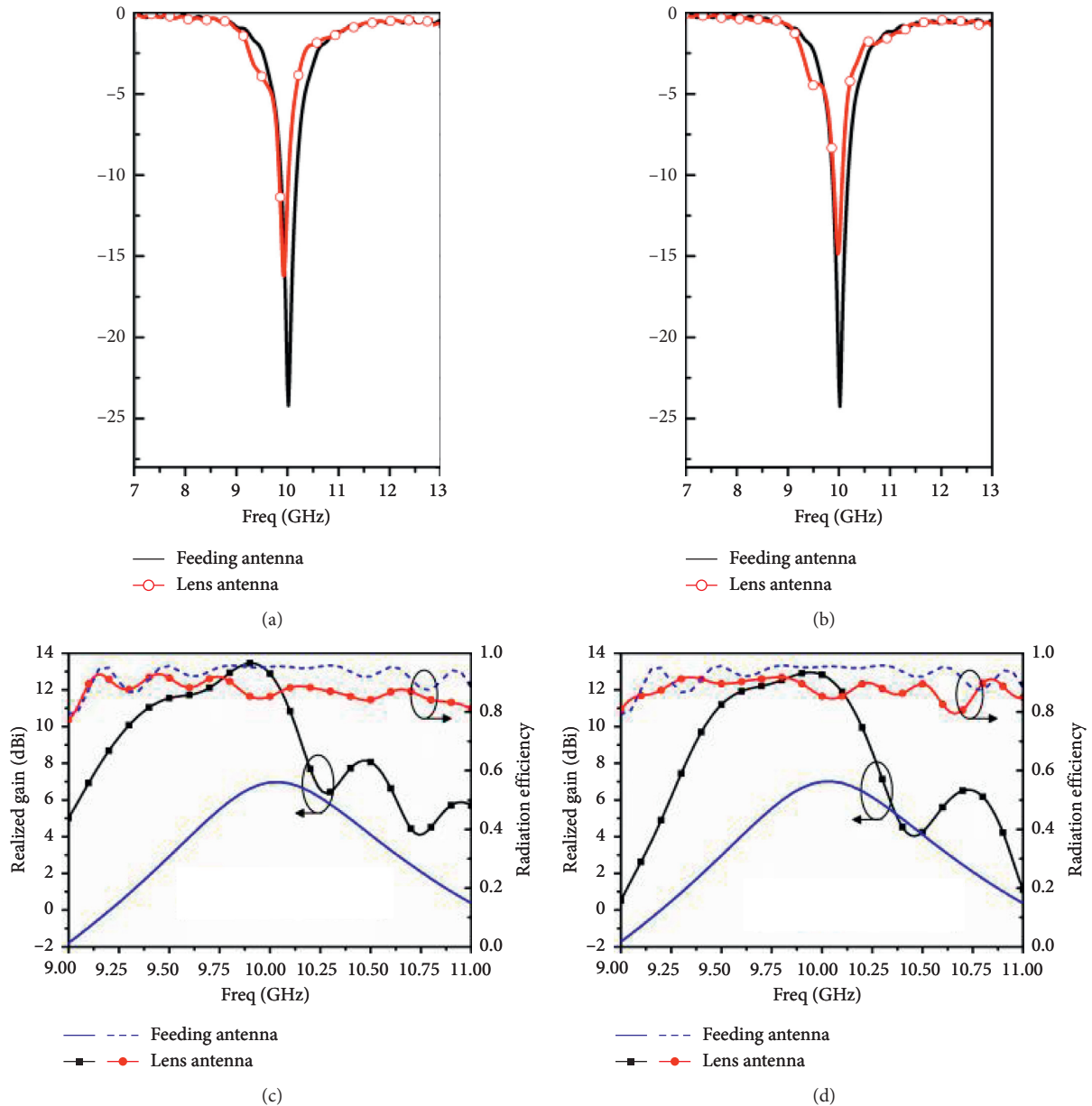


FIGURE 15: Frequency-dependent magnitudes of input reflection coefficients, main lobe gain, and radiation efficiency of the freestanding microstrip patch antenna element and the R-type cylindrical metasurface lens antenna. (a, c) TE-polarized radiation. (b, d) TM-polarized radiation.

antenna need suppression by further optimization of the configuration of R-type operation.

#### 4. Experimental Verification

Although the transmission-focusing and reflection-focusing differentiate the operating manners of the T-type and R-type cylindrical metasurface lenses, both lenses share a similar design and simulation procedures mentioned above. Therefore, only the cylindrical metasurface lens antenna operating in T-type is fabricated and measured in this section so as to verify the simulation-based observations. The aforementioned commercial laminates and foam are used

for the prototype. The metasurface lens fabricated through printed circuit board (PCB) technology is attached to the cylindrical surface by plastic screws with M2 thread size. A photograph of the prototype under measurement is provided in Figure 17. The measured input reflection coefficient of the lens antenna and its frequency-dependent boresight gain are already shown in Figures 12. The operating frequency around 10 GHz is observed for both polarizations. Besides, Figure 13 also presents the measured radiation patterns in  $xy$ - and  $xz$ -planes for both polarizations at 10 GHz. The measured boresight gains for TE- and TM-polarized radiation, which are obtained through the comparison with a horn antenna with known gain, are 17.07 dBi

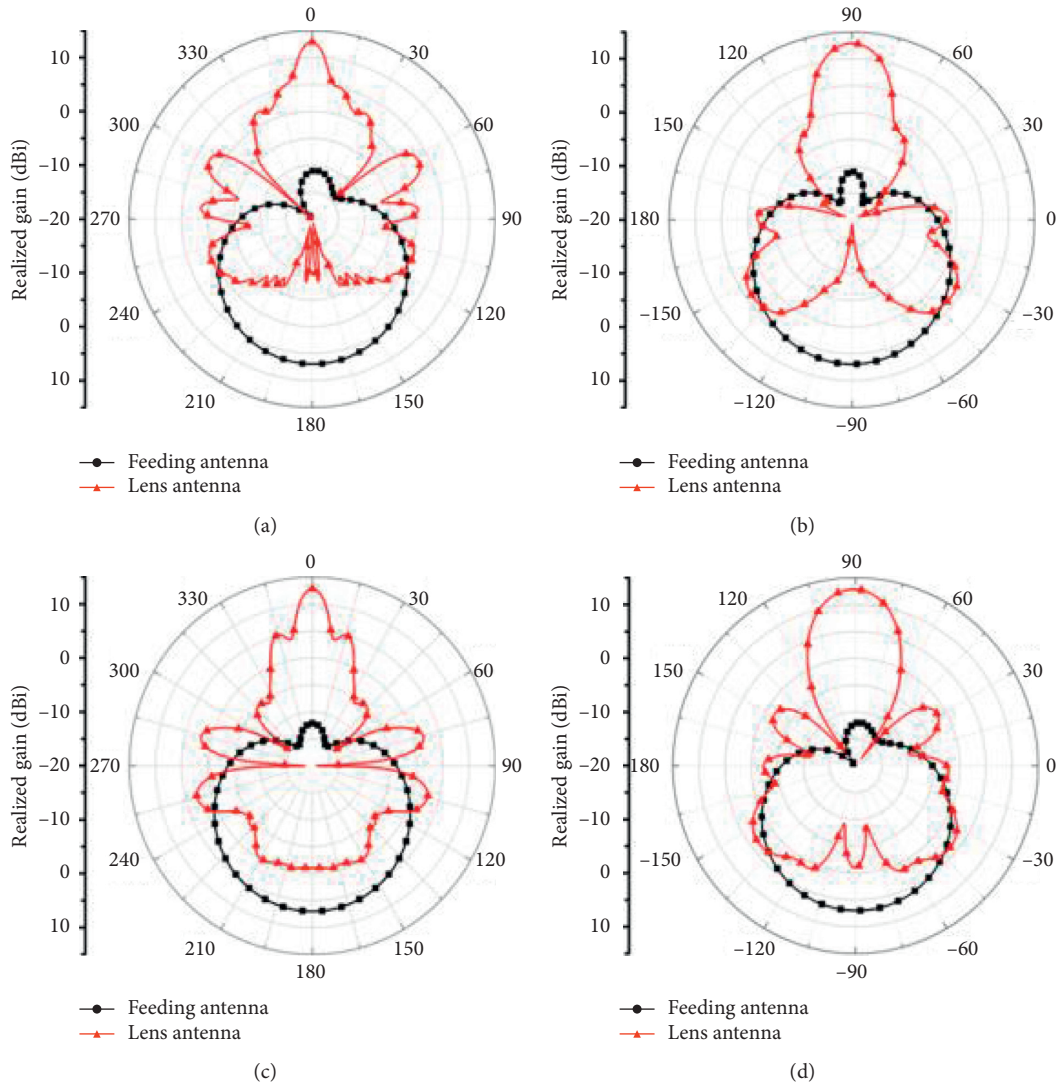


FIGURE 16: Simulated two-dimensional radiation patterns of the freestanding microstrip patch antenna element and the R-type cylindrical metasurface lens antenna. (a)  $xy$ - and (b)  $xz$ -planes for TE-polarized radiation and (c)  $xy$ - and (d)  $xz$ -planes for TM-polarized radiation.

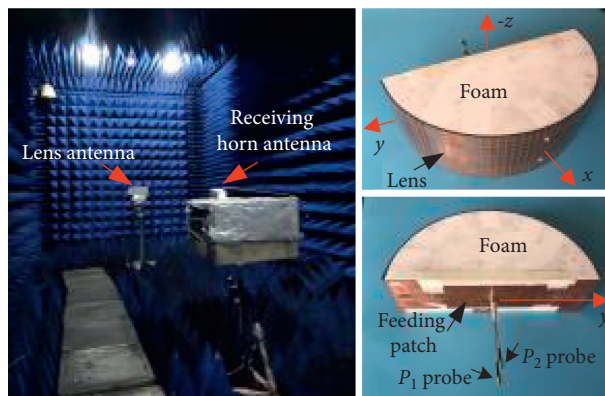


FIGURE 17: Photo of the measurement setup of the T-type cylindrical metasurface lens antenna.

and 18.62 dBi, respectively. Compared with the simulation, the 1.28 dB and 0.24 dB difference in boresight gain for TE and TM polarizations as well as the difference between

simulated and measured patterns may be attributed to the tolerances introduced by the manual assembly of the three separate dielectric layers of the lens, positioning of the

feeding antenna, and collimation between the prototype and receiving horn antenna. In particular, the collimation between the lens antenna under the test and the receiving horn antenna is accomplished with visual inspection. Besides, the antennas are manually turned by ninety degrees during the measurement of different planes and polarizations. Those factors account for the collimation tolerance which may also lead to the slight difference in main lobe peaks in  $xy$ - and  $xz$ -planes for the same polarization since the lens antenna exhibits the main lobe with narrow beamwidth in  $xy$ -plane. Overall, the agreement between simulation and measurement is observed for the input reflection coefficient and radiation pattern, which validates the presented design.

## 5. Conclusions

Cylindrical metasurface lenses with a thin radial profile have been presented to serve as an example of demonstrating the conformal integration or embedment of the electromagnetic lens towards the cylindrical shell of certain platform bodies. The conformal integration or embedment potentially ensures the undisturbed local shape as well as aerodynamics of the platform, which can hardly be achieved during direct integration of the traditional lens or planar metasurface lens onto a cylindrical skin. Based on the calculation and sampling of the phase gradient, transmission or reflection phase distribution of the cylindrical metasurface lens was determined for implementation. In order to relatively independently tune the TM and TE responses for oblique incidence, the basic and simple slot or loop geometry has been, respectively, employed as the unit cell of the T-type or R-type cylindrical metasurface lens. Other compact geometries that meet the consideration of tuning can be also used to construct the unit cell of the lens with dual-polarization capability. Due to the control of refraction or reflection, focused beam of each cylindrical lens has been observed. In comparison with the freestanding feeding antenna, enhanced boresight gain has been obtained from each cylindrical lens antenna for both TE- and TM-polarized radiation at the operating frequency. Meanwhile, certain limitations including the side lobe of the T-type cylindrical lens antenna, back lobe of the R-type cylindrical lens antenna, and narrow-band operation of the lenses are also observed. Introducing a certain gradient for focusing effect along the axial direction of the cylinder to reduce the side lobe level and using other unit cell design schemes with a smaller period to widen the operating bandwidth of the lenses may be exploited in a future study [41, 42]. In addition, avoiding the scattering into undesired directions by implementing the phase and amplitude distribution during the design of unit cells may also be considered to improve the antenna efficiency [43]. Furthermore, presented designs suggest a potential of the lens to be conformally integrated or embedded into the cylindrical structure of certain airborne or spaceborne platforms which may possess a cylinder-like component part, for the sake of the enhanced boresight gain without an obvious increase of drag for the moving platforms.

## Data Availability

The data used to support the findings of this study are available from the corresponding author upon request.

## Conflicts of Interest

The authors declare that there are no conflicts of interest regarding the publication of this paper.

## Acknowledgments

This work was supported in part by the National Natural Science Foundation of China under Grant 61601379 and Grant 61771407 and in part by the Fundamental Research Funds for the Central Universities under Grant 2682018CX41.

## References

- [1] E. Jones, "Paraboloid reflector and hyperboloid lens antennas," *Transactions of the IRE Professional Group on Antennas and Propagation*, vol. 2, no. 3, pp. 119–127, 1954.
- [2] P. Uslenghi, "On the generalized Luneburg lenses," *IEEE Transactions on Antennas and Propagation*, vol. 17, no. 5, pp. 644–645, 1969.
- [3] T. A. Rhys, "The design of radially symmetric lenses," *IEEE Transactions on Antennas and Propagation*, vol. 18, no. 4, pp. 497–506, 1970.
- [4] N. Yu, P. Genevet, M. A. Kats et al., "Light propagation with phase discontinuities: generalized laws of reflection and refraction," *Science*, vol. 334, no. 6054, pp. 333–337, 2011.
- [5] N. Yu and F. Capasso, "Flat optics with designer metasurfaces," *Nature Materials*, vol. 13, no. 2, pp. 139–150, 2014.
- [6] H. Shi, J. Li, A. Zhang et al., "Gradient metasurface with both polarization-controlled directional surface wave coupling and anomalous reflection," *IEEE Antennas and Wireless Propagation Letters*, vol. 14, pp. 104–107, 2015.
- [7] S. Sun, K.-Y. Yang, C.-M. Wang et al., "High-efficiency broadband anomalous reflection by gradient meta-surfaces," *Nano Letters*, vol. 12, no. 12, pp. 6223–6229, 2012.
- [8] Y. Li, J. Zhang, S. Qu et al., "Wideband radar cross section reduction using two-dimensional phase gradient metasurfaces," *Applied Physics Letters*, vol. 104, no. 22, p. 221110, 2014.
- [9] C. Huang, W. Pan, X. Ma, and X. Luo, "Wideband radar cross-section reduction of a stacked patch array antenna using metasurface," *IEEE Antennas and Wireless Propagation Letters*, vol. 14, pp. 1369–1372, 2015.
- [10] Y.-C. Song, J. Ding, C.-J. Guo, Y.-H. Ren, and J.-K. Zhang, "Ultra-broadband backscatter radar cross section reduction based on polarization-insensitive metasurface," *IEEE Antennas and Wireless Propagation Letters*, vol. 15, pp. 329–331, 2016.
- [11] C. Pfeiffer and A. Grbic, "Bianisotropic metasurfaces for optimal polarization control: analysis and synthesis," *Physical Review Applied*, vol. 2, no. 4, Article ID 044011, 2014.
- [12] Y. Li, J. Zhang, S. Qu et al., "Achieving wide-band linear-to-circular polarization conversion using ultra-thin bi-layered metasurfaces," *Journal of Applied Physics*, vol. 117, no. 4, Article ID 044501, 2015.
- [13] T. Cai, G.-M. Wang, X.-F. Zhang et al., "Ultra-thin polarization beam splitter using 2-D transmissive phase gradient

- metasurface," *IEEE Transactions on Antennas and Propagation*, vol. 63, no. 12, pp. 5629–5636, 2015.
- [14] H. C. Chou, N.-L. Tung, and M. Ng Mou Kehn, "The double-focus generalized luneburg lens design and synthesis using metasurfaces," *IEEE Transactions on Antennas and Propagation*, vol. 66, no. 9, pp. 4936–4941, 2018.
- [15] E. Arbabi, A. Arbabi, S. M. Kamali, Y. Horie, and A. Faraon, "High efficiency double-wavelength dielectric metasurface lenses with dichroic birefringent meta-atoms," *Optics Express*, vol. 24, no. 16, pp. 18468–18477, 2016.
- [16] S. Wang, X. Wang, Q. Kan et al., "Spin-selected focusing and imaging based on metasurface lens," *Optics Express*, vol. 23, no. 20, pp. 26434–26441, 2015.
- [17] Q. Yang, J. Gu, D. Wang et al., "Efficient flat metasurface lens for terahertz imaging," *Optics Express*, vol. 22, no. 21, pp. 25931–25939, 2014.
- [18] X. Li, S. Xiao, B. Cai, Q. He, T. J. Cui, and L. Zhou, "Flat metasurfaces to focus electromagnetic waves in reflection geometry," *Optics Letters*, vol. 37, no. 23, pp. 4940–4942, 2012.
- [19] A. Pors, M. G. Nielsen, R. L. Eriksen, and S. I. Bozhevolnyi, "Broadband focusing flat mirrors based on plasmonic gradient metasurfaces," *Nano Letters*, vol. 13, no. 2, pp. 829–834, 2013.
- [20] W. Ma, D. Jia, X. Yu et al., "Reflective gradient metasurfaces for polarization-independent light focusing at normal or oblique incidence," *Applied Physics Letters*, vol. 108, no. 7, Article ID 071111, 2016.
- [21] W. Yao, L. Tang, J. Wang, C. Ji, X. Wei, and Y. Jiang, "Spectrally and spatially tunable terahertz metasurface lens based on graphene surface plasmons," *IEEE Photonics Journal*, vol. 10, no. 4, pp. 1–8, 2018.
- [22] Y. Shi, K. Li, J. Wang, L. Li, and C.-H. Liang, "An etched planar metasurface half Maxwell fish-eye lens antenna," *IEEE Transactions on Antennas and Propagation*, vol. 63, no. 8, pp. 3742–3747, 2015.
- [23] M. Bosiljevac, M. Casaletti, F. Caminita, Z. Sipus, and S. Maci, "Non-uniform metasurface Luneburg lens antenna design," *IEEE Transactions on Antennas and Propagation*, vol. 60, no. 9, pp. 4065–4073, 2012.
- [24] H. Zhu, S. W. Cheung, and T. I. Yuk, "Enhancing antenna boresight gain using a small metasurface lens: reduction in half-power beamwidth," *IEEE Antennas and Propagation Magazine*, vol. 58, no. 1, pp. 35–44, 2016.
- [25] A. H. Abdelrahman, A. Z. Elsherbeni, and F. Fan Yang, "High-gain and broadband transmitarray antenna using triple-layer spiral dipole elements," *IEEE Antennas and Wireless Propagation Letters*, vol. 13, pp. 1288–1291, 2014.
- [26] H. Li, G. Wang, H.-X. Xu, T. Cai, and J. Liang, "X-band phase-gradient metasurface for high-gain lens antenna application," *IEEE Transactions on Antennas and Propagation*, vol. 63, no. 11, pp. 5144–5149, 2015.
- [27] H. Li, G. Wang, J. Liang, X. Gao, H. Hou, and X. Jia, "Single-layer focusing gradient metasurface for ultrathin planar lens antenna application," *IEEE Transactions on Antennas and Propagation*, vol. 65, no. 3, pp. 1452–1457, 2017.
- [28] T. Cai, G.-M. Wang, J.-G. Liang, Y.-Q. Zhuang, and T.-J. Li, "High-performance transmissive meta-surface for lens antenna application," *IEEE Transactions on Antennas and Propagation*, vol. 65, no. 7, pp. 3598–3606, 2017.
- [29] Y. Han, J. Zhang, Y. Li et al., "Miniaturized-element offset-feed planar reflector antennas based on metasurfaces," *IEEE Antennas and Wireless Propagation Letters*, vol. 16, pp. 282–285, 2017.
- [30] H.-P. Li, G.-M. Wang, T. Cai, J.-G. Liang, and X.-J. Gao, "Phase-and amplitude-control metasurfaces for antenna main-lobe and sidelobe manipulations," *IEEE Transactions on Antennas and Propagation*, vol. 66, no. 10, pp. 5121–5129, 2018.
- [31] H.-X. Xu, S. Tang, G.-M. Wang et al., "Multifunctional microstrip array combining a linear polarizer and focusing metasurface," *IEEE Transactions on Antennas and Propagation*, vol. 64, no. 8, pp. 3676–3682, 2016.
- [32] T. Cai, G.-M. Wang, X.-L. Fu, J.-G. Liang, and Y.-Q. Zhuang, "High-efficiency metasurface with polarization-dependent transmission and reflection properties for both reflectarray and transmitarray," *IEEE Transactions on Antennas and Propagation*, vol. 66, no. 6, pp. 3219–3224, 2018.
- [33] H.-P. Li, G.-M. Wang, X.-J. Gao, J.-G. Liang, and H.-S. Hou, "A novel metasurface for dual-mode and dual-band flat high-gain antenna application," *IEEE Transactions on Antennas and Propagation*, vol. 66, no. 7, pp. 3706–3711, 2018.
- [34] X. Yan, L. Liang, J. Yang et al., "Broadband, wide-angle, low-scattering terahertz wave by a flexible 2-bit coding metasurface," *Optics Express*, vol. 23, no. 22, pp. 29128–29137, 2015.
- [35] Y. Zhang, L. Liang, J. Yang et al., "Broadband diffuse terahertz wave scattering by flexible metasurfaces with randomized phase distribution," *Scientific Reports*, vol. 6, p. 26875, 2016.
- [36] Y. Shang and Z. Shen, "Polarization-independent backscattering enhancement of cylinders based on conformal gradient metasurfaces," *IEEE Transactions on Antennas and Propagation*, vol. 65, no. 5, pp. 2386–2396, 2017.
- [37] L. Matekovits and T. S. Bird, "Width-modulated microstrip-line based mantle cloaks for thin single- and multiple cylinders," *IEEE Transactions on Antennas and Propagation*, vol. 62, no. 5, pp. 2606–2615, 2014.
- [38] Y. R. Padooru, A. B. Yakovlev, P.-Y. Chen et al., "Analytical modeling of conformal mantle cloaks for cylindrical objects using subwavelength printed and slotted arrays," *Journal of Applied Physics*, vol. 112, no. 3, Article ID 034907, 2012.
- [39] N. M. Estakhri and A. Alù, "Ultra-thin unidirectional carpet cloak and wavefront reconstruction with graded metasurfaces," *IEEE Antennas and Wireless Propagation Letters*, vol. 13, pp. 1775–1778, 2014.
- [40] A. H. Abdelrahman, A. Z. Elsherbeni, and F. Yang, "Transmission phase limit of multilayer frequency-selective surfaces for transmitarray designs," *IEEE Transactions on Antennas and Propagation*, vol. 62, no. 2, pp. 690–697, 2014.
- [41] K. Liu, Y. Ge, and C. Lin, "A compact wideband high-gain metasurface-lens-corrected conical horn antenna," *IEEE Antennas and Wireless Propagation Letters*, vol. 18, no. 3, pp. 457–461, 2019.
- [42] J.-J. Liang, G.-L. Huang, J.-N. Zhao, Z.-J. Gao, and T. Yuan, "Wideband phase-gradient metasurface antenna with focused beams," *IEEE Access*, vol. 7, pp. 20767–20772, 2019.
- [43] A. Epstein and G. V. Eleftheriades, "Huygens' metasurfaces via the equivalence principle: design and applications," *Journal of the Optical Society of America B*, vol. 33, no. 2, pp. A31–A50, 2016.